Journal of Biomedical Optics

BiomedicalOptics.SPIEDigitalLibrary.org

Rotational imaging optical coherence tomography for full-body mouse embryonic imaging

Chen Wu
Narendran Sudheendran
Manmohan Singh
Irina V. Larina
Mary E. Dickinson
Kirill V. Larin

SPIE.

Rotational imaging optical coherence tomography for full-body mouse embryonic imaging

Chen Wu,[a,†] Narendran Sudheendran,[a,†] Manmohan Singh,[a] Irina V. Larina,[b] Mary E. Dickinson,[b] and Kirill V. Larin[a,b,c,*]
[a]University of Houston, Department of Biomedical Engineering, Houston, 3605 Cullen Boulevard, Texas 77204, United States
[b]Baylor College of Medicine, Department of Molecular Physiology and Biophysics, One Baylor Plaza, Houston, Texas 77584, United States
[c]Tomsk State University, Interdisciplinary Laboratory of Biophotonics, 36 Lenin Avenue, Tomsk 634050, Russia

Abstract. Optical coherence tomography (OCT) has been widely used to study mammalian embryonic development with the advantages of high spatial and temporal resolutions and without the need for any contrast enhancement probes. However, the limited imaging depth of traditional OCT might prohibit visualization of the full embryonic body. To overcome this limitation, we have developed a new methodology to enhance the imaging range of OCT in embryonic day (E) 9.5 and 10.5 mouse embryos using rotational imaging. Rotational imaging OCT (RI-OCT) enables full-body imaging of mouse embryos by performing multiangle imaging. A series of postprocessing procedures was performed on each cross-section image, resulting in the final composited image. The results demonstrate that RI-OCT is able to improve the visualization of internal mouse embryo structures as compared to conventional OCT. [DOI: 10.1117/1.JBO.21.2.026002]

Keywords: optical coherence tomography; rotational imaging optical coherence tomography; mammalian embryos; imaging.

Paper 150752PR received Nov. 6, 2015; accepted for publication Jan. 7, 2016; published online Feb. 5, 2016.

1 Introduction

Genetic and environmental factors are well known to cause congenital diseases during embryonic development. Animal models such as *Drosophila*,[1] zebrafish,[2] *Xenopus*,[3] and mice[4,5] are commonly used to study human diseases. Mouse embryos have been particularly useful in studying human congenital diseases as they are mammals, share almost 85% of their genes with humans, have a three-week gestation period, are relatively inexpensive to maintain, and are available as numerous transgenic and mutant models.[6–8] A current challenge is to develop an imaging modality that can be used to noninvasively study dynamic changes in morphology and function in three dimensions (3-D) within living embryos with high spatial and temporal resolution.

Traditionally, histology has been used to obtain high-resolution and high-contrast images of the embryos. However, histology cannot be used to image live embryos, and obtaining full 3-D images is very challenging.[9,10] More recently, imaging modalities such as confocal microscopy, optical projection tomography (OPT), ultrasound biomicroscopy (UBM), micro-magnetic resonance imaging (micro-MRI), and optical coherence tomography (OCT) have been employed to acquire 3-D images of living mouse embryos.[11–15] Confocal microscopy can acquire images with excellent spatial resolution (<1 μm) but has an imaging depth of ~100 to 200 μm, which restricts its ability to image deeper regions of a mouse embryo.[11,16] In contrast, UBM can image deeper structures in mouse embryos.[13,17] However, UBM spatial resolution is limited to ~30 to 100 μm and has poor contrast in comparison with optical imaging modalities. Monitoring dynamic changes in developing embryos is challenging using micro-MRI as it requires extended acquisition periods (~2 h) to obtain images with acceptable contrast, which makes live imaging particularly challenging because of movement artifacts.[14] OPT can obtain high-resolution 3-D images of embryos with exquisite detail and contrast, but it requires lengthy immobilization and clearing procedures for fixed mouse embryos.[12,18,19] While live OPT imaging of a mouse embryo has been demonstrated, only a limb bud was imaged.[20]

OCT has emerged as a powerful technique to image a wide range of biological tissues.[21,22] OCT can achieve ~2 to 10 μm resolution and an imaging depth of ~1 to 2 mm in turbid media such as tissue with excellent intrinsic contrast. Recent developments in OCT technology have enabled real-time video-rate four-dimensional imaging at up to 1 GVoxel/s.[23] Because of its noninvasive nature, rapid imaging speed, nondestructive near-infrared illumination, and micrometer-scale spatial resolution, OCT has widely been used for murine embryonic imaging.[15,24,25] Our group has previously demonstrated *in utero* and *in vivo* applications of OCT to study different aspects of murine embryo development, such as in cardiovascular,[26,27] ocular,[15] limb,[24] and brain[28] tissue. Despite continuous progress in OCT technology development, imaging depth remains a major challenge, limiting visualization of mouse embryos older than E9.5 (embryonic day 9.5—days after a vaginal plug was found) with OCT. Although imaging depth can be improved, it is often at the expense of resolution. Full-range OCT has been developed to increase the imaging range by introducing a carrier frequency and removing the complex conjugate artifact;[29] however, this technique also suffers from strong light attenuation for nontransparent biological tissues.

We have previously demonstrated that optical clearing can enhance OCT imaging depth in mouse embryos.[30] However, effective optical clearing techniques are not compatible yet

*Address all correspondence to: Kirill V. Larin, E-mail: klarin@uh.edu

†Equally contributed to this work.

1083-3668/2016/$25.00 © 2016 SPIE

with live imaging. Thus, we have developed a method to obtain a complete 3-D structure of a mouse embryo with OCT called rotational imaging OCT (RI-OCT).[31] During data acquisition, conventional 3-D OCT imaging was performed at four different angles: 0 deg, 90 deg, 180 deg, and 270 deg. During postprocessing, the data sets were coregistered into a single 3-D image. Results demonstrate that RI-OCT can be used to obtain the complete 3-D structure of mouse embryo at E9.5 and E10.5, which previously could not be accomplished using conventional OCT imaging.

2 Materials and Methods

2.1 *Experimental Setup*

The experimental setup consists of a commercial swept-source OCT (SS-OCT) system (Thorlabs, MEMS-VCSEL OCS1310V2) and a square glass tube mounted on a rotational stage to hold the embryo. A schematic representation of the experimental setup is shown in Fig. 1. The SS-OCT system has a central wavelength of 1300 nm, bandwidth of 100 nm, and A-scan rate of 200 kHz. The axial resolution of the SS-OCT system was ~12 μm, and the transverse resolution was ~15 μm. The imaging depth of the system was ~6 mm, and the depth of focus was ~1 mm, both in air. The quartz tubes utilized in this study were custom-made by Precision Cell Inc. The tube used for E9.5 embryo imaging had an outer width of 5 mm and inner width of 4 mm. The tube used for the E10.5 embryo had an outer width of 7 mm and inner width of 5 mm. The refractive index of the glass was measured as 1.5.

The laser beam was scanned across the sample using galvanometer-mounted mirrors. The 3-D axes (x, y, and z) are depicted in the inset of Fig. 1. Here, a B-scan [two-dimensional (2-D) image] is set along the xz-plane, which is the horizontal plane. The stage is rotated around the y-axis during RI-OCT image acquisition.

2.2 *Mouse Embryo Preparation*

Timed matings of CD-1 mice were set up overnight and checked for vaginal plugs on the following morning. The day on which the vaginal plug was observed was recorded as E0.5. Mouse embryos were dissected at the E9.5 stage (9.5 days after a vaginal plug was found) with the yolk sac intact. The embryos were transferred to the square glass tube, which was filled with 0.9% saline solution for imaging. In order to demonstrate the capability of this technique for live embryonic imaging, mouse embryos at the E10.5 stage were dissected and kept alive in a culturing medium in a controlled incubator environment.[27] All procedures were approved by UH IACUC.

2.3 *Rotational Imaging Optical Coherence Tomography Imaging Procedure*

The embryo was placed within the square tube with the coronal and sagittal planes parallel to the walls of the glass tube. This minimized the propagation distance of the OCT probe beam through the embryo, which subsequently decreased light attenuation. The glass tube surface was aligned with the imaging system as shown in Fig. 1, and conventional 3-D OCT images were acquired at four different angles of rotation (0 deg, 90 deg, 180 deg, and 270 deg).

2.3.1 *Square tube alignment*

The square tube was first placed on the rotational stage as shown in Fig. 1. The image acquisition flow chart is shown in Fig. 2(a). First, the glass surface was aligned to be almost normal to the OCT probe beam to reduce any image artifacts due to refraction. The glass surface was set slightly off normal to the beam to avoid direct reflections from the glass surface and subsequent saturation artifacts. Then the tube was aligned so that the embryo was within the field of view (FOV) of the OCT imaging system at all four RI-OCT imaging angles.

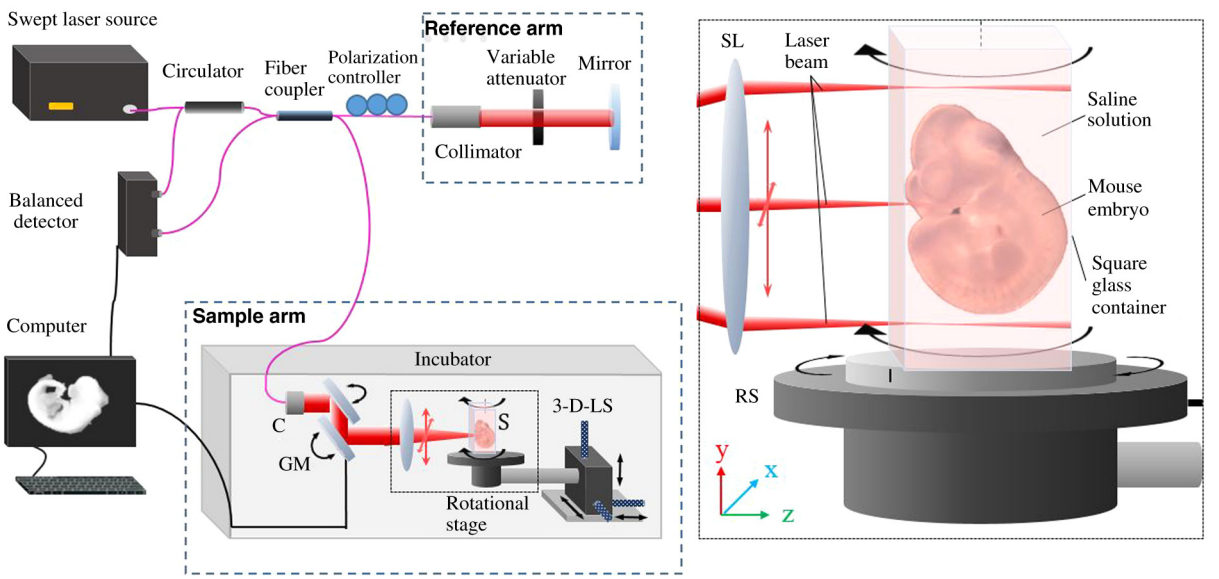

Fig. 1 Schematic diagram for RI-OCT system. C, collimator; RS, rotational stage; SL, scan lens; LS, linear stage; GM, galvo mirrors.

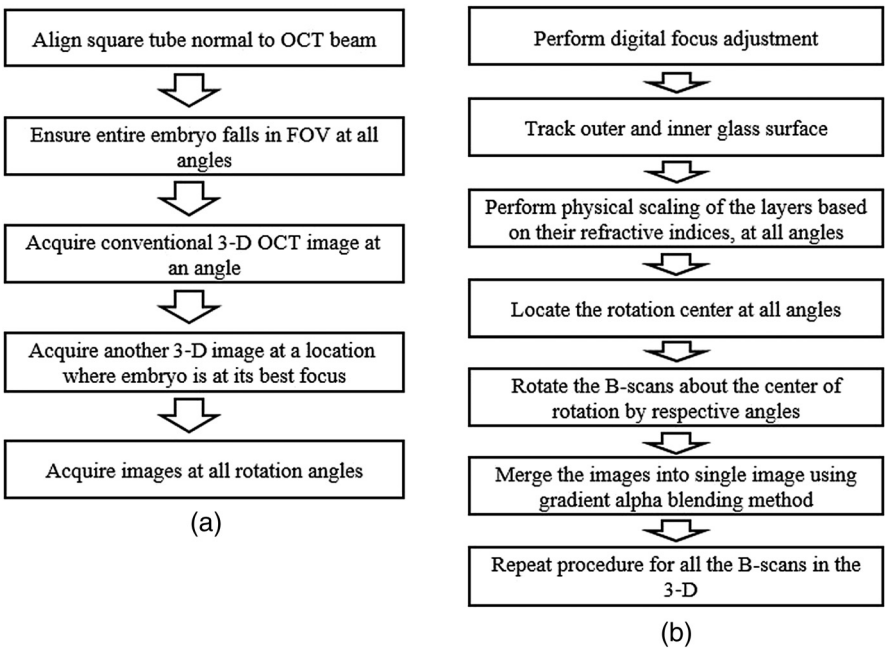

Fig. 2 RI-OCT procedure for (a) imaging acquisition and (b) image construction.

2.3.2 *Image acquisition*

Image acquisition was performed once the glass tube was aligned. As shown in Fig. 3(a), if the embryo was out of focus at a particular RI-OCT imaging angle, a conventional 3-D image was acquired at the original location. Next, the embryo was brought into focus and another 3-D image was acquired. Then, the embryo was moved back to its original location and the stage was rotated by 90 deg. The entire process was repeated for four orthogonal angles of 0 deg, 90 deg, 180 deg, and 270 deg.

2.4 *Rotational Imaging Optical Coherence Tomography Image Registration*

An algorithm was developed to register the data sets obtained at four angles into a single 3-D image (described below).

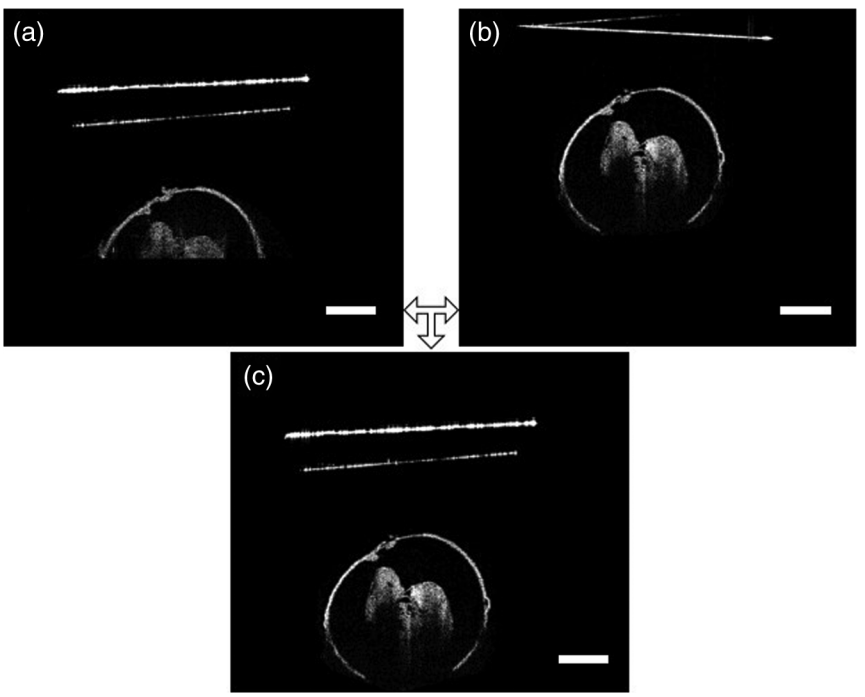

Fig. 3 The OCT images (a) before adjustment, (b) after adjustment, and (c) combination. Scale bars are 500 μm.

2.4.1 *Digital focus adjustment*

As mentioned above, conventional 3-D OCT images were acquired for every rotation angle at the original position as well as the position where the embryo is in focus. These two images are shown in Figs. 3(a) and 3(b), respectively. In this step, the image of the embryo at its original location was replaced with the image of the in-focus embryo. The resulting image is depicted in Fig. 3(c). Figure 3(c) shows how the in-focus embryo depicted in Fig. 3(b) is replaced by the in-position embryo in Fig. 3(a). This process is repeated for each of the four RI-OCT acquisition angles.

2.4.2 *Physical scaling*

Because OCT relies on the optical path difference between the sample and the reference mirror, OCT images are scaled based on the respective refractive indices of the individual components of the sample. Therefore, the images were rescaled to their correct physical dimensions. Each B-scan was divided into regions based on refractive indices. The outer and inner glass surfaces were traced first. The region above the glass tube's outer surface is composed of air with a refractive index of 1. The region of the glass tube wall is assigned a refractive index of 1.5. The region below the glass tube's inner surface is comprised of saline and the embryo, and the average refractive index was assigned as 1.38. This procedure was performed on images from all four angles.

2.4.3 *Locating center of rotation*

Although the glass tube was carefully aligned with respect to the rotation stage, perfect adjustment of the center of the tube along the axis of rotation of the stage is difficult due to the effect of the optical path. This implies that the center of rotation had to be computed from the OCT B-scans. To accomplish this, a point which could be tracked in two B-scans, before and after rotation, was used to determine the rotation center. In Fig. 4(a), a point marked as (x_1, y_1) in the OCT B-scan at 0 deg could be tracked and is marked as (x_2, y_2) in the OCT B-scan obtained after rotation by 90 deg. Let (x_1, y_1) and (x_2, y_2) be the points before and after rotation by 90 deg, respectively, about an unknown center of rotation (m, n), as shown in Fig. 4(c). The coordinates are defined with respect to the center of the image, (0,0). The point after rotation (x_2, y_2) can be obtained from the initial point (x_1, y_1) rotated about an arbitrary point (m, n) by angle θ by the following relation:

$$\begin{bmatrix} x_2 - m \\ y_2 - n \end{bmatrix} = \begin{bmatrix} \cos\theta & \sin\theta \\ -\sin\theta & \cos\theta \end{bmatrix} \begin{bmatrix} x_1 - m \\ y_1 - n \end{bmatrix}. \quad (1)$$

By using $\theta = 90$ deg, Eq. (1) can be simplified as

$$m = (-x_1 + x_2 - y_1 - y_2)/2, \quad (2)$$

$$n = (-x_1 - x_2 + y_1 - y_2)/2. \quad (3)$$

The rotation center (m, n) can therefore be determined using Eqs. (2) and (3).

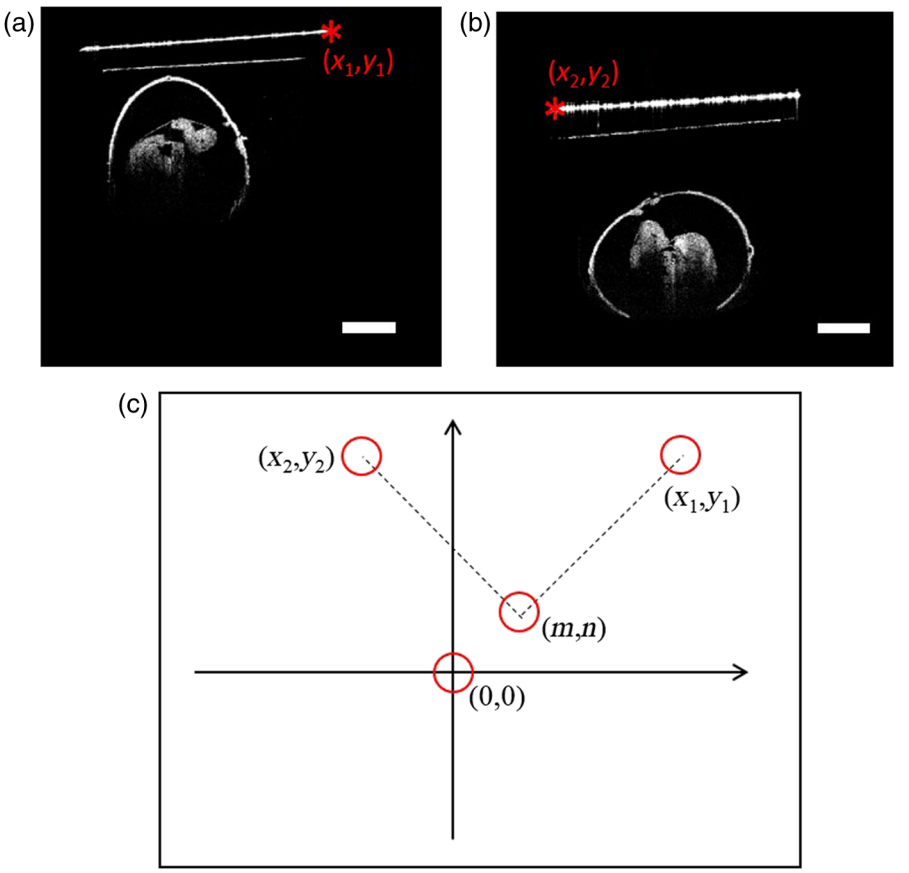

Fig. 4 Locating the center of rotation. (a) Image acquired from 0 deg; (b) image acquired from 90 deg; (c) the coordinates from the same position (corner of the tube) and rotation center. Scale bars are 500 μm.

2.4.4 *Merging images*

Once the center of rotation (m, n) was determined, the B-scans obtained at different angles were rotated about (m, n) by the respective angle of rotation. These individual images were then merged to form a single B-scan by gradient alpha blending (feathering).[32] First, the overlap between two opposing individual images (I_A and I_B) was identified, and then the pixel values in the blended regions were weighted and averaged from the two overlapping images by the coefficients α (alpha mask) which varied as a function of the distance from the seam, described as

$$I_{com}(i, j) = \alpha I_A(i, j) + (1 - \alpha) I_B(i, j). \quad (4)$$

The gradient blending method minimized the effects of intensity variations on the registration. The entire process was performed on all the B-scans in the 3-D OCT stack.

3 Results

The typical B-scan and 3-D rendering of a mouse embryo at E9.5 obtained using OCT are shown in Figs. 5(a) and 5(b), respectively. The effect of light attenuation in depth is clearly

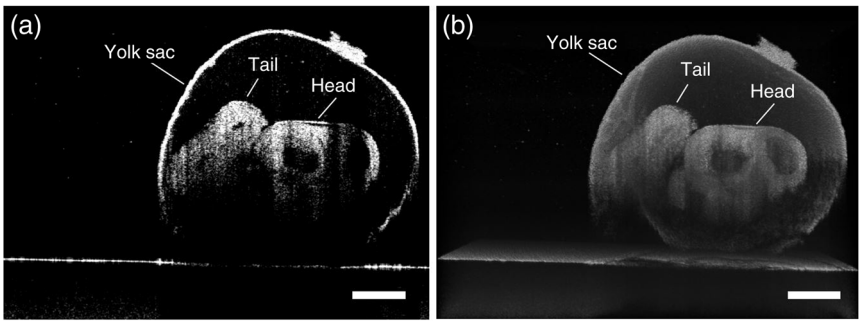

Fig. 5 (a) Cross-section image of the E9.5 mouse embryo and (b) 3-D OCT rendering of the same embryo. Scale bars are 500 μm.

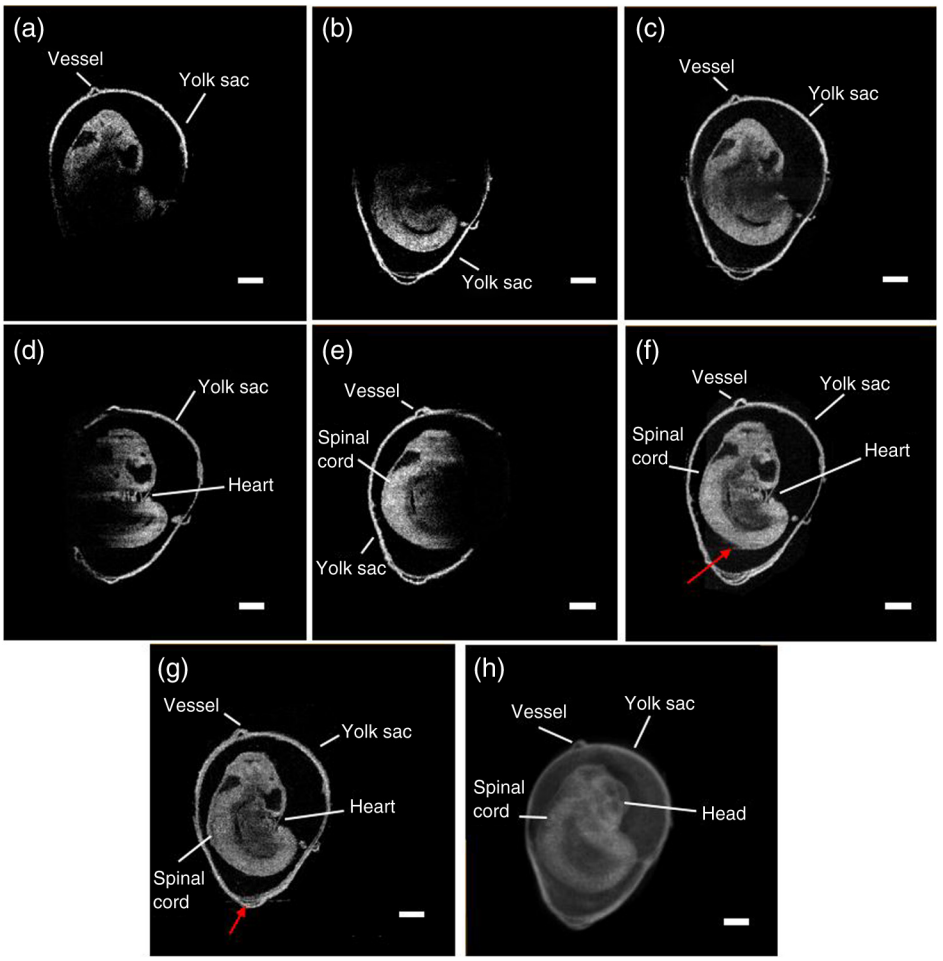

Fig. 6 Selected OCT image at (a) 0 deg, (b) 180 deg, (c) 0 deg and 180 deg composite, (d) 90 deg, (e) 270 deg, (f) 0 deg and 180 deg composite, (g) composite from all four angles, (h) corresponding 3-D rendering for the composite from all four angles of an E9.5 embryo. Scale bars are 500 μm.

seen. The head and the tail of the embryo are still visible in the image, but the structures below them cannot be seen due to attenuation and subsequent shadowing. Figure 6 demonstrates the rotational imaging approach for the same embryo. Figures 6(a), 6(b), 6(d), and 6(e) depict selected cross-sectional OCT images obtained from different angles. The rendering was performed using Amira software. Figures 6(c), 6(f), and 6(g) were obtained by combining OCT images from 0 deg and 180 deg, 90 deg and 270 deg, and all four angles, respectively. Figure 6(h) is a 3-D projection of the embryo for the combined image from all four angles. In the RI-OCT composite obtained from the images acquired at 90 deg and 180 deg, shown in Fig. 6(f), fine structures within the embryo heart are clearly resolvable. Various structures became visible after application of RI-OCT, such as the yolk sac, head, spinal cord, heart, and yolk sac vessels. However, these structures are not resolvable from the composite obtained from 0 deg and 180 deg, as depicted in Fig. 6(c). The cross-sectional and 3-D projection images of the E10.5 stage embryo from one angle and combined angles are shown in Fig. 7. The complete brain cavity structure is difficult to discern from a single angle, but it can be clearly visualized in the combined images. Some structures were blurred due to the decidua. In the 3-D projection view, the embryo and yolk sac structures are labeled as different colors for better visualization. The head and tail are only visible after combining the images. Figure 7(e) is a selected frame from the video of a E10.5 mouse embryo heartbeat. The heartbeat video was recorded for 4 s at a frame rate of 250 Hz after RI-OCT imaging. In total, seven heartbeats were observed during this period, which corresponds to a heartbeat of ~105 beats/min and corroborates with previous work.[33] 3-D RI-OCT images of both the E9.5 and E10.5 mouse embryos are shown in Videos 1 and 2.

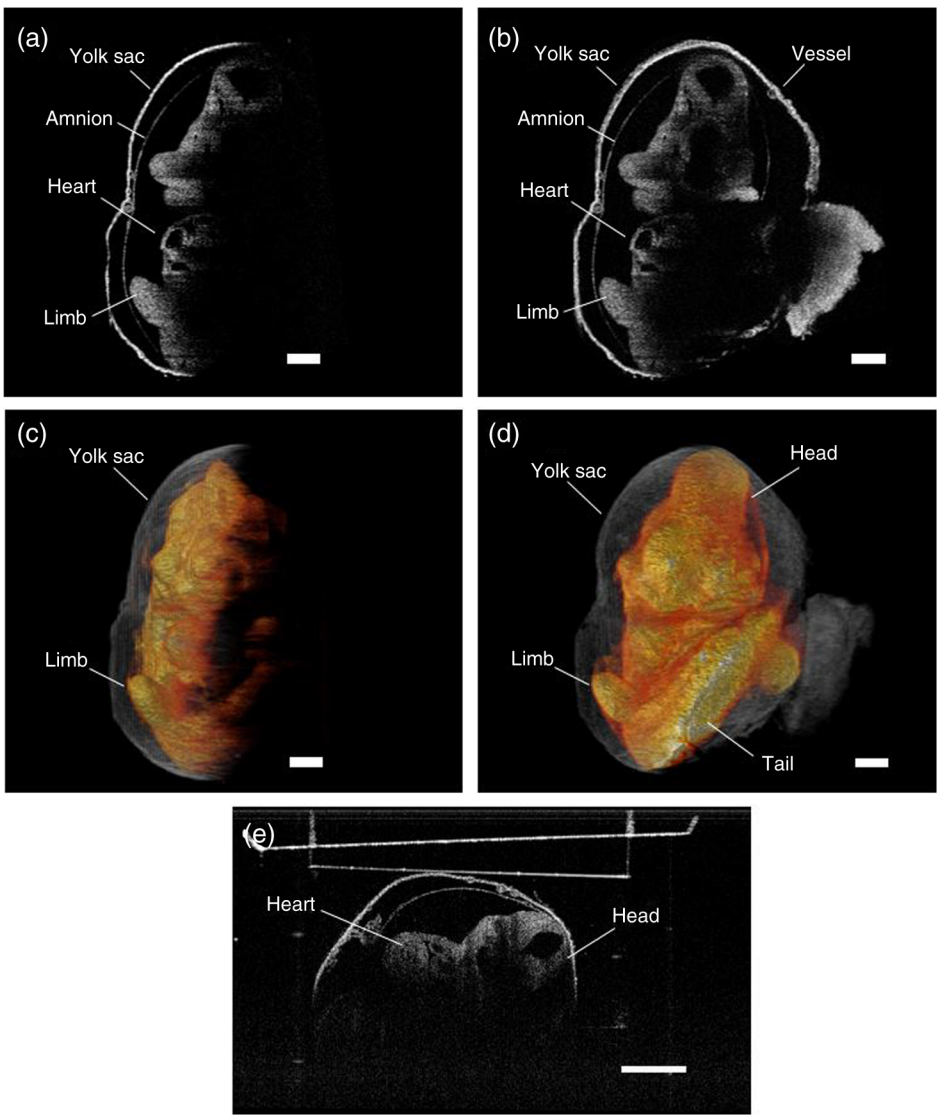

Fig. 7 Selected OCT image: (a) at 0 deg, (b) composite from all four angles, (c) 3-D rendering at 0 deg, (d) 3-D rendering from all four angles, (e) a video frame of the heartbeat of an E10.5 embryo. Scale bars are 500 μm. Video 1, MP4, 14.7 MB [URL: http://dx.doi.org/10.1117/1.JBO.21.2.026002.1]; Video 2, MPG, 21.3 MB [URL: http://dx.doi.org/10.1117/1.JBO.21.2.026002.2]; Video 3, MPG, 11.5 MB [URL: http://dx.doi.org/10.1117/1.JBO.21.2.026002.3].

4 Discussion

OCT can capture structural and functional information from embryos of various animal models with high spatial and temporal resolution and contrast. The main disadvantage of using conventional 3-D OCT structural imaging is the loss of signal and imaging contrast of deeper structures due to light attenuation. Figure 3(b) shows that the deeper structures of a E9.5 mouse embryo within an intact yolk sac cannot be resolved by traditional OCT, even when the sample is in focus. This necessitates the development of new imaging methods that can be used to obtain complete structural information of the mouse embryo. Here we presented a straightforward imaging protocol and registration algorithm, referred to as RI-OCT, to overcome this challenge.

As described in this work, the imaging protocol requires conventional 3-D OCT images of the in-focus embryo at four orthogonal angles: 0 deg, 90 deg, 180 deg, and 270 deg. This procedure ensured that structural information from different parts of the embryo was captured. Using the registration algorithm, images from different angles were reconstructed into a single 3-D structural image (first introduced in Ref. 34). The main advantage of this approach is that it overcomes the limited imaging depth of OCT by retrieving structural information from multiple perspectives. A similar concept has also been applied to mouse embryo cardiac phenotyping.[35] In our current setup, a small tilt is introduced between the glass surface and the beam (to avoid specular reflection from the glass surface) that might lead to imperfect overlapping of the images during the registration process. In the future, antireflection coating on the glass surface could reduce specular reflections and minimize the incidence angle. Furthermore, the concavity or convexity of the glass tube will result in convergence or divergence of the OCT probe beam, resulting in imprecise reconstruction of the embryonic structures. Hence, we have utilized a square glass tube to reduce imaging deformation. Precautions should be taken to avoid any displacement of the embryo during this step in order to minimize blurring and inaccurate registration of the final composited RI-OCT image. There are several methods to help ensure stabilization of the mouse embryo during RI-OCT imaging such as tying a piece of hair around the ectoplacental cone region on the top of the yolk sac so the weight and length of the hair can limit the motion or using customized cuvettes which more precisely match the dimension of embryos at various stages.

The first step during the RI-OCT image registration process (Sec. 2.4) is digital focus registration (Sec. 2.4.1). The glass surface and the embryo must be displaced only along the optical axis. To obtain the correct physical dimensions and locations of the glass tube and the embryo, it is imperative to correctly estimate the refractive index of the glass, saline, and the embryo. This will ensure that the proper physical dimensions are obtained and utilized in the registration process. The final step is to determine the center of rotation accurately from the images as described in Sec. 2.4.3. The center of rotation was determined using images obtained from successive rotation steps. After rotation of the B-scan images from different angles with respect to the calculated center coordinates, a slight translational offset might be needed to ensure accurate overlapping of the images.

By comparing the combined images [Figs. 6(c), 6(f), and 6(g)] to the single perspective images [Figs. 6(a), 6(b), 6(d), and 6(e)], the benefit of RI-OCT is evident. Since in-focus imaging was performed at each angle, embryonic structures imaged at the corresponding angles are clearly visualized in the combined image. For example, the head and tail of the embryo are well defined in Fig. 6(c), but fine heart structures are blurred because the heart was positioned deep within the embryo when it was imaged at 0 deg and 180 deg. However, the heart was superficially positioned at 270 deg, so the heart structures were well resolved as seen in Fig. 6(f). On the other hand, careful inspection of the regions marked by the red arrows in Figs. 6(f) and 6(g) shows that although the general outline and large structures of the embryo were reconstructed well, there is blurring at the edges due to imperfect overlap in some regions. This suggests that there were minute errors during the image acquisition and registration process, which may not be entirely resolvable. The initial alignment of the cuvette relative the imaging beam is also very important for the final registration. The accuracy of the alignment could be improved by, for example, placing an agar phantom containing microbeads as a base for the mouse embryo inside the cuvette, which can be used similarly as the guiding stars. The appearance of the same microbeads in images taken at the different angles would ensure that the same cross section of the sample was imaged. In this work, a gradient alpha blending method was used to merge the images, but application of more sophisticated image registration techniques would also improve the image quality of the final composited images.

In general, RI-OCT is able to access deeper embryonic structures as compared to conventional OCT due to multiangle illumination and imaging. However, due to the light attenuation, the imaging depth range of any method is inherently limited. Several approaches have been proposed to improve the imaging depth of OCT, such as tissue clearing[30,36] and light attenuation compensation of the OCT signal.[37,38] While optical clearing can significantly enhance imaging depth, it is challenging to apply for live embryos due to toxicity effects. Direct application of light attenuation compensation algorithms to OCT images results in abnormally high pixel intensities and noise at greater depths, which makes it unsuitable for RI-OCT. Figure 7 shows the capability of RI-OCT for conducting live mouse embryonic imaging. The current method of whole mouse embryo culture is only able to support live *in vitro* development of E5.5 to E9.5 embryos for a period of up to 24 to 48 h. It is not yet feasible to extend embryonic development *in vitro* beyond the organogenesis stages;[39] and therefore mouse embryos younger than E10.5 would be more suitable for imaging with this technique.

Due to its benefits of whole-body imaging of mouse embryos, RI-OCT could be a powerful tool for phenotyping embryonic structural abnormalities in genetically engineered mice to study developmental diseases such as brain malformation[40,41] and congenital heart defects.[42–44] The noninvasive nature, relatively rapid imaging speed, and minimal computational complexity means that RI-OCT can provide high-throughput imaging for large-scale phenotyping projects that heavily rely on evaluating phenotypic outcomes.

5 Conclusion

In this study, we have demonstrated a new method to visualize a whole E9.5 and E10.5 mouse embryo within its intact yolk sac by combining traditional 3-D OCT images obtained at different angles. From the final RI-OCT, the whole embryo and yolk sac structure can be visualized. The results demonstrate that RI-OCT was able to significantly improve the OCT imaging

depth and contrast of the deep structures of mouse embryos, which can benefit future embryonic investigations. RI-OCT could also be combined with other techniques such as speckle variance for functional analysis of deeper structures, which traditional OCT imaging would be unable to image. In addition, the proposed RI-OCT technique is not limited to mouse embryonic research; it can also be extended to other biomedical research fields which encounter similar issues of light attenuation and which could partially be ameliorated by the application of multi-angle imaging techniques.

Acknowledgments

This work was funded by NIH HL077187, HL095586, U54 HG006348-S1, T32 HL007676, and NIH R01HL120140.

References

1. U. B. Pandey and C. D. Nichols, "Human disease models in Drosophila melanogaster and the role of the fly in therapeutic drug discovery," *Pharmacol. Rev.* **63**(2), 411–436 (2011).
2. K. Dooley and L. I. Zon, "Zebrafish: a model system for the study of human disease," *Curr. Opin. Genet. Dev.* **10**(3), 252–256 (2000).
3. A. Ny et al., "A genetic *Xenopus laevis* tadpole model to study lymphangiogenesis," *Nat. Med.* **11**(9), 998–1004 (2005).
4. S. Batzoglou et al., "Human and mouse gene structure: comparative analysis and application to exon prediction," *Genome. Res.* **10**(7), 950–958 (2000).
5. A. I. Su et al., "A gene atlas of the mouse and human protein-encoding transcriptomes," *Proc. Natl. Acad. Sci. U. S. A.* **101**(16), 6062–6067 (2004).
6. S. D. Brown et al., "The functional annotation of mammalian genomes: the challenge of phenotyping," *Annu. Rev. Genet.* **43**, 305–333 (2009).
7. J. Graw, "Mouse models of congenital cataract," *Eye* **13**, 438–444 (1999).
8. D. M. Juriloff and M. J. Harris, "Mouse models for neural tube closure defects," *Hum. Mol. Genet.* **9**(6), 993–1000 (2000).
9. L. W. Crawford, J. F. Foley, and S. A. Elmore, "Histology atlas of the developing mouse hepatobiliary system with emphasis on embryonic days 9.5-18.5," *Toxicol. Pathol.* **38**(6), 872–906 (2010).
10. M. G. Carter et al., "Mice deficient in the candidate tumor suppressor gene Hic1 exhibit developmental defects of structures affected in the Miller-Dieker syndrome," *Hum. Mol. Genet.* **9**(3), 413–419 (2000).
11. A. L. Lopez, III et al., "Live confocal microscopy of the developing mouse embryonic yolk sac vasculature," *Methods. Mol. Biol.* **1214**, 163–172 (2015).
12. J. Sharpe et al., "Optical projection tomography as a tool for 3D microscopy and gene expression studies," *Science* **296**(5567), 541–545 (2002).
13. F. S. Foster et al., "In vivo imaging of embryonic development in the mouse eye by ultrasound biomicroscopy," *Invest. Ophthalmol. Vis. Sci.* **44**(6), 2361–2366 (2003).
14. B. Hogers et al., "Magnetic resonance microscopy of mouse embryos in utero," *Anat. Rec.* **260**(4), 373–377 (2000).
15. I. V. Larina et al., "Optical coherence tomography for live phenotypic analysis of embryonic ocular structures in mouse models," *J. Biomed. Opt.* **17**(8), 081410 (2012).
16. R. M. Zucker, E. S. Hunter, III, and J. M. Rogers, "Apoptosis and morphology in mouse embryos by confocal laser scanning microscopy," *Methods* **18**(4), 473–480 (1999).
17. D. H. Turnbull et al., "Ultrasound backscatter microscope analysis of early mouse embryonic brain development," *Proc. Natl. Acad. Sci. U. S. A.* **92**(6), 2239–2243 (1995).
18. J. R. Walls et al., "Three-dimensional analysis of vascular development in the mouse embryo," *PLoS One* **3**(8), e2853 (2008).
19. M. Singh et al., "Comparison of optical projection tomography and optical coherence tomography for assessment of murine embryonic development," *Proc. SPIE* **9334**, 93340J (2015).
20. J.-F. Colas and J. Sharpe, "Live optical projection tomography," *Organogenesis* **5**(4), 211–216 (2009).
21. M. R. Hee et al., "Optical coherence tomography of the human retina," *Arch. Ophthalmol.* **113**(3), 325–332 (1995).
22. D. Huang et al., "Optical coherence tomography," *Science* **254**(5035), 1178–1181 (1991).
23. W. Wieser et al., "High definition live 3D-OCT in vivo: design and evaluation of a 4D OCT engine with 1 GVoxel/s," *Biomed. Opt. Express.* **5**(9), 2963–2977 (2014).
24. S. H. Syed et al., "Optical coherence tomography for high-resolution imaging of mouse development in utero," *J. Biomed. Opt.* **16**(4), 046004 (2011).
25. N. Sudheendran et al., "Speckle variance OCT imaging of the vasculature in live mammalian embryos," *Laser Phys. Lett.* **8**(3), 247 (2011).
26. I. V. Larina et al., "Live imaging of blood flow in mammalian embryos using Doppler swept-source optical coherence tomography," *J. Biomed. Opt.* **13**(6), 060506 (2008).
27. S. Wang et al., "Direct four-dimensional structural and functional imaging of cardiovascular dynamics in mouse embryos with 1.5 MHz optical coherence tomography," *Opt. Lett.* **40**(20), 4791–4794 (2015).
28. N. Sudheendran et al., "Comparative assessments of the effects of alcohol exposure on fetal brain development using optical coherence tomography and ultrasound imaging," *J. Biomed. Opt.* **18**(2), 020506 (2013).
29. L. An, M. Hrebesh, and R. K. Wang, "Full range complex spectral domain optical coherence tomography for volumetric imaging at 47,000 A scans per second," *J. Opt.* **12**(8), 84003 (2010)
30. I. V. Larina et al., "Enhanced OCT imaging of embryonic tissue with optical clearing," *Laser Phys. Lett.* **5**(6), 476–480 (2008).
31. N. Sudheendran et al., "Rotational imaging OCT for full-body embryonic imaging," *Proc. SPIE* **8934**, 89342K (2014).
32. V. Rankov et al., "An algorithm for image stitching and blending," *Proc. SPIE*, **5701**, 190–199 (2005).
33. B. B. Keller et al., "In vivo assessment of embryonic cardiovascular dimensions and function in day-10.5 to -14.5 mouse embryos," *Circ. Res.* **79**(2), 247–255 (1996).
34. N. Sudheendran et al., "Enhancing imaging depth by multi-angle imaging of embryonic structures," *Proc. SPIE* **8953**, 895306 (2014).
35. M. Cua et al., "Morphological phenotyping of mouse hearts using optical coherence tomography," *J. Biomed. Opt.* **19**(11), 116007 (2014).
36. D. Zhu et al., "Recent progress in tissue optical clearing," *Laser Photonics Rev.* **7**(5), 732–757 (2013).
37. M. J. Girard et al., "Shadow removal and contrast enhancement in optical coherence tomography images of the human optic nerve head," *Invest. Ophthalmol. Vis. Sci.* **52**(10), 7738–7748 (2011).
38. J. M. Mari et al., "Enhancement of lamina cribrosa visibility in optical coherence tomography images using adaptive compensation," *Invest. Ophthalmol. Vis. Sci.* **54**(3), 2238–2247 (2013).
39. P. P. Tam, "Postimplantation mouse development: whole embryo culture and micro-manipulation," *Int. J. Dev. Biol.* **42**(7), 895–902 (1998).
40. A. Kasarskis, K. Manova, and K. V. Anderson, "A phenotype-based screen for embryonic lethal mutations in the mouse," *Proc. Natl. Acad. Sci. U. S. A.* **95**(13), 7485–7490 (1998).
41. T. E. Willnow et al., "Defective forebrain development in mice lacking gp330/megalin," *Proc. Natl. Acad. Sci. U. S. A.* **93**(16), 8460–8464 (1996).
42. M. W. Jenkins et al., "Phenotyping transgenic embryonic murine hearts using optical coherence tomography," *Appl. Opt.* **46**(10), 1776–1781 (2007).
43. X. Liu et al., "Imaging techniques for visualizing and phenotyping congenital heart defects in murine models," *Birth. Defects. Res. C. Embryo. Today.* **99**(2), 93–105 (2013).
44. G. Karunamuni et al., "Using optical coherence tomography to rapidly phenotype and quantify congenital heart defects associated with prenatal alcohol exposure," *Dev. Dyn.* **244**(4), 607–618 (2015).

Chen Wu received his BS degree in optical information science and technology from Ocean University of China in 2010 and his MS degree in biomedical engineering from Martin Luther University Halle-Wittenberg in Germany in 2013. Currently, he is a PhD candidate in the Department of Biomedical Engineering at the University of Houston. His research interests are in the development of optical coherence tomography technique and the application in different biomedical fields such embryonic imaging, ophthalmology, and tissue biomechanics.

Narendran Sudheendran received his PhD in biomedical engineering at the University of Houston. He obtained his master's degree in electrical engineering from the University of Houston. His research focuses mainly on using optical coherence tomography (OCT) in embryology. His other interests include angiography and algorithm development.

Manmohan Singh received his BS degree in biomedical engineering from the University of Houston in 2014. He is currently pursuing his PhD in the Department of Biomedical Engineering, also at the University of Houston. Since the fall of 2010, he has been with Dr. Kirill Larin's Biomedical Optics Laboratory. His research interests include utilizing biomedical imaging for the detection and monitoring of diseases and utilizing and developing new elastographic methods for investigating the biomechanical properties of tissues.

Irina V. Larina has received her MS degree in physics from Saratov State University in Russia in 1996 and her PhD degree in physiology and biophysics from the University of Texas Medical Branch at Galveston in 2005. She is an assistant professor at the Department of Molecular Physiology and Biophysics at the Baylor College of Medicine and a codirector of the optical imaging and vital microscopy core. Her research focuses on development of novel methods for intravital, optical imaging of reproductive and developmental events in mouse models, and using these methods to understand normal development and the nature of congenital defects in humans.

Mary E. Dickinson received her MA, MS, and PhD in biological sciences from Columbia University in 1996. She is a professor of molecular physiology and biophysics at Baylor College of Medicine, an adjunct professor in bioengineering at Rice University, and she holds the Kyle and Josephine Morrow Endowed Chair. She is the academic director of the optical imaging and vital microscopy core and an executive member of the Cardiovascular Research Institute (CVRI). Her work focuses on the development of 3D and 4D imaging methods to define genetic and biomechanical mechanisms underlying malformations associated with congenital birth defects.

Kirill V. Larin is a professor of biomedical engineering at the University of Houston. He received his first MS in laser physics and mathematics from Saratov State University (1995), his second MS in cellular physiology and molecular biophysics in 2001, and a PhD in biomedical engineering in 2002 from the University of Texas Medical Branch in Galveston. His research contributions are in biomedical optics and biophotonics and development and application of various optical methods for noninvasive and nondestructive imaging and diagnostics of tissues and cells. He is a fellow of SPIE and OSA.